

Atacama Cosmology Telescope: Observations of supermassive black hole binary candidates

Strong sinusoidal variations at 95, 147 and 225 GHz in PKS 2131–021 and PKS J0805–0111

Adam D. Hincks^{1,2}, Xiaoyi Ma (马潇依)^{3,4}, Sigurd K. Naess⁵, Sebastian Kiehlmann⁶, Przemek Mróz⁷,
J. Richard Bond⁸, Mark Devlin⁹, Jo Dunkley^{10,11}, Allen Foster¹⁰, Matthew J. Graham¹², Yilun Guan¹³,
Carlos Hervías-Caimapo¹⁴, John C. Hood II¹⁵, Michael D. Niemack^{16,17}, John Orlowski-Scherer⁹,
Lyman A. Page¹⁰, Bruce Partridge¹⁸, Anthony C. S. Readhead¹⁹, Cristóbal Sifón²⁰, Suzanne T. Staggs¹⁰, and
Cristian Vargas²¹

¹ David A. Dunlap Department of Astronomy & Astrophysics, University of Toronto, 50 St. George St., Toronto ON M5S 3H4, Canada

² Specola Vaticana (Vatican Observatory), V-00120 Vatican City State

³ Kavli Institute for Astronomy & Astrophysics, Peking University, Beijing 100871, People's Republic of China

⁴ Department of Astronomy, School of Physics, Peking University, Beijing 100871, People's Republic of China

⁵ Institute of Theoretical Astrophysics, University of Oslo, Norway

⁶ Institute of Astrophysics, Foundation for Research & Technology-Hellas, GR-71110 Heraklion, Greece

⁷ Astronomical Observatory, University of Warsaw, Al. Ujazdowskie 4, 00-478 Warszawa, Poland

⁸ Canadian Institute for Theoretical Astrophysics, University of Toronto, 60 St. George Street, Toronto, ON M5S 3H8, Canada

⁹ Department of Physics & Astronomy, University of Pennsylvania, 209 South 33rd Street, Philadelphia, PA, 19104, USA

¹⁰ Joseph Henry Laboratories of Physics, Jadwin Hall, Princeton University, Princeton, NJ, USA 08544

¹¹ Department of Astrophysical Sciences, Peyton Hall, Princeton University, Princeton, NJ USA 08544

¹² Division of Physics, Mathematics, and Astronomy, California Institute of Technology, Pasadena, CA 91125, USA

¹³ Dunlap Institute for Astronomy & Astrophysics, University of Toronto, 50 St. George St., Toronto ON M5S 3H4, Canada

¹⁴ Instituto de Astrofísica & Centro de Astro-Ingeniería, Facultad de Física, Pontificia Universidad Católica de Chile, Av. Vicuña Mackenna 4860, 7820436 Macul, Santiago, Chile

¹⁵ Department of Astronomy & Astrophysics, University of Chicago, 5640 South Ellis Avenue, Chicago, IL, USA 60637

¹⁶ Department of Physics, Cornell University, Ithaca, NY 14853, USA

¹⁷ Department of Astronomy, Cornell University, Ithaca, NY 14853, USA

¹⁸ Department of Physics & Astronomy, Haverford College, Haverford, PA, USA 19041

¹⁹ Owens Valley Radio Observatory, California Institute of Technology, Pasadena, CA 91125, USA

²⁰ Instituto de Física, Pontificia Universidad Católica de Valparaíso, Casilla 4059, Valparaíso, Chile

²¹ Mitchell Institute for Fundamental Physics & Astronomy and Department of Physics & Astronomy, Texas A&M University, College Station, Texas 77843, USA

April 8, 2025

ABSTRACT

Large sinusoidal variations in the radio light curves of the blazars PKS J0805–0111 and PKS 2131–021 have recently been discovered with an 18-year monitoring programme by the Owens Valley Radio Observatory, making these systems strong supermassive black hole binary (SMBHB) candidates. The sinusoidal variations in PKS 2131–021 dominate its light curves from 2.7 GHz to optical frequencies. We report sinusoidal variations observed in both objects with the Atacama Cosmology Telescope (ACT) at 95, 147 and 225 GHz consistent with the radio light curves. The ACT 95 GHz light curve of PKS 2131–021 agrees well with the contemporaneous 91.5 GHz ALMA light curve and is comparable in quality. Broadband, intermittent, sinusoidal variations are also observed in PKS J0805–0111, for which there are no ALMA or other millimetre light curves, showing that PKS 2131–021 is not an isolated case and that these three properties could be common in blazar SMBHB phenomenology. In both blazars the sinusoid phase as a function of frequency as well as the achromaticity of the sinusoid amplitudes are consistent with the expected signature of jets in SMBHB systems. Monitoring of ~8000 blazars by the Simons Observatory over the next decade should provide a large number of SMBHB candidates that will shed light on the nature of the nanohertz gravitational-wave background.

Key words. Galaxies: active - Galaxies: jets - quasars: supermassive black holes

1. Introduction

Evidence of a stochastic background of gravitational waves (GW) with periods of months to years has recently been presented by the North American Nanohertz Observatory for Gravitational Waves collaboration (Agazie et al. 2023a) and the European Pulsar Timing Array collaboration (EPTA Collaboration 2023); the MeerKAT Pulsar Timing Array collaboration also find evidence for the background, but caution that is highly dependent on choices in their noise modelling (Miles et al. 2025). The only method of searching for GW at these wavelength scales uses millisecond pulsar timing arrays (MsPTAs; Readhead & Hewish 1974; Backer et al. 1982).¹ Supermassive black hole binary systems (SMBHBs) have been suggested as the origin of this stochastic background (e.g., Agazie et al. 2023a,b), making clear the importance of searches for their electromagnetic counterparts.

Supermassive black holes (SMBHs) drive the central engines in active galactic nuclei (AGN), which are strong sources of emission across the electromagnetic spectrum (Krolik & Di Matteo 2000; Blandford et al. 2019). Since 2008 the 40 m Telescope of the Owens Valley Radio Observatory (OVRO) has been dedicated full time to monitoring ~1830 blazars at 15 GHz on a 3–4 day cadence (Richards et al. 2011). Of the ~1830 blazars monitored, 1158 comprise a complete sample suitable for statistical tests. To date, two AGN with sinusoidal variations dominating their light curves have been identified in this sample, which rigorous statistical tests show are unlikely to be produced by random fluctuations in the red noise tail of their power spectral density (PSD): PKS 2131–021 (O’Neill et al. 2022, hereafter referred to as O22; Kiehlmann et al. 2024, hereafter K24) and PKS J0805–0111 (De la Parra et al. 2024, hereafter D24). K24 and D24 simulated 10^6 light curves that match the PSD and probability density functions (PDF; i.e., the flux distribution) of PKS 2131–021 and PKS J0805–0111, and showed that the joint global probability, p , of these two sources, out of the sample of 1158, being generated randomly due to the red noise tail in their variability spectra is $p < 3 \times 10^{-3}$ (D24).

It is by no means obvious that orbital motion of a SMBH with a relativistic jet will produce sinusoidal variations; however, a mechanism was discovered independently by Sobacchi et al. (2017) and by O22, which K24 refer to as the ‘Kinetic Orbital’ (KO) model. In the KO model, one of the SMBHs in the binary system produces a jet, and aberration of this jet due to orbital motion has a large effect on the observed emission from the highly relativistic emitting material. This is shown in O22 to produce sinusoidal variations.

In addition to studying radio light curves, K24 analysed publicly available light curves of PKS 2131–021 at millimetre (mm), infrared and optical frequencies and found the same sine wave pattern in them all, as well as ‘hints’ of a sinusoid at γ -ray frequencies. This broad-band signal is explained well by the KO model since the orbital aberration affects all frequencies. The light curves exhibited a

monotonic phase shift in the sine waves as a function of frequency from the radio to the optical, spanning more than five decades in frequency. This can be interpreted as an optical depth effect in which the higher frequencies probe closer to the central engine, a behaviour that has been observed in many blazars since it was discovered in the first maps made with very long baseline interferometry (Readhead et al. 1978; Readhead 1980). Although the light travel time between the higher-frequency and lower-frequency zones corresponds to several sinusoidal cycles, the jet itself is travelling at close to the speed of light. Thus, by the time the higher-frequency light arrives at the location of the lower-frequency emission, the jet material lags behind only slightly, leading to a relatively small phase delay in the observed light curve.

In this paper we report observations with the Atacama Cosmology Telescope (ACT) of PKS 2131–021 and PKS J0805–0111 from 2016 to 2022 at 95, 147 and 225 GHz that provide new insights into these two objects, the phenomenology of SMBHBs in blazars, and the potential for wide-field CMB surveys to discover scores of SMBHB candidates and determine their periods. In principle, the velocity and phase could be obtained from optical light curves of mm-discovered SMBHB, since the optical signal is believed to originate close to the AGN core and would therefore be virtually in phase with the SMBHB orbit. One could then mount coherent GW searches with MsPTAs – i.e., searches at known frequencies and phases rather than within stochastic noise – thus potentially expanding their reach to weaker sources of GW.

The paper is organised as follows. In Sec. 2 we describe the ACT light curves and briefly introduce other, ancillary data used in our analyses. In Sec. 3, we present sinusoidal fits to the ACT light curves of PKS 2131–021 and PKS J0805–0111, and in Sec. 4, we analyse and discuss the relative phase shifts between light curves at different frequencies as well as the achromaticity of the sinusoidal amplitudes. In Sec. 5, we discuss the promise of mm observations of AGN for future SMBHB candidate discoveries, comparing and contrasting to optical searches. We summarise our findings and conclude in Sec. 6.

2. Data

2.1. The ACT observations

ACT was a cosmic microwave background (CMB) experiment that operated from 2007 to 2022 in the Atacama Desert of Chile. Its 6 m telescope observed with three generations of receivers: the Millimeter Bolometric Array Camera (MBAC, 2007–11; Swetz et al. 2011), ACTPol (2013–15; Thornton et al. 2016) and Advanced ACTPol (2016–22; Henderson et al. 2016). All receivers were equipped with three optics tubes, each terminating in its own array of detectors that were occasionally changed to allow different combinations of frequencies to be observed. Starting with ACTPol, detectors were polarisation-sensitive and, beginning with the fourth polarised array (PA4), were also dichroic, i.e., sensitive to two frequency bands. Collectively, PA1 to PA7 observed in five frequency bands: f030, f040, f090, f150 and f220. The two lowest frequencies are still being analysed, and all science results so far, including in this paper, come from f090, f150 and f220, whose band centres for a synchrotron spectral index of -0.7 , averaged across

¹ There were two crucial steps in the discovery of millisecond pulsars: (i) the discovery of interplanetary scintillation, at Galactic latitude -0.3° , in 4C 21.53 by Readhead & Hewish (1974) (see Readhead 2024), which drew attention to the singular nature of this object; and (ii) the discovery of millisecond pulses from 4C 21.53W by Backer et al. (1982).

the PAs, were 95.0, 147.1 and 225.0 GHz, respectively.² See Hervías-Caimapo et al. (2024) for a full summary of the array timelines and frequencies. The passbands are discussed in Madhavacheril et al. (2020) and Coulton et al. (2024).

A paper presenting the ACT bright AGN sample is in preparation (Ma et al.), and the light curve data will be publicly released. The data reduction process and an analysis of calibration uncertainties and other error sources will be described more fully in that paper and here we introduce only the essentials. Light curves are generated by creating $2 \times 2 \text{ deg}^2$ maps centred on the source for each day the source was observed. Data are calibrated from raw readout units to incident power by measuring the detector response to small, square-wave changes in the voltage bias applied to the detectors (Niemack 2008); this is performed at least hourly. Interdetector calibration is achieved by flat fielding on the atmospheric emission which creates a common signal mode across the detectors. Calibration from incident power to celestial flux density is achieved using observations of Uranus that were taken every few nights and a final correction based on cross correlating ACT and *Planck* angular power spectra is applied.³ See Choi et al. (2020) and Naess et al. (2025) for more information on the general map-making process. With the individual maps in hand, the point source flux density is extracted from each with a matched filter using the known telescope beams and a noise covariance estimated from the map itself after masking the source, similar to the method of Marriage et al. (2011), except that individual pixel weights are also accounted for in the noise covariance.⁴ The resulting light curves tend to have a few outlying points, almost all of which are automatically flagged as outliers by our pipeline due to the low effective number of detectors in the receiver for a particular observation (e.g., because of bad weather, or because the source was near the edge of the observed field). A small fraction of data points, $\sim 0.1\%$, are flagged as outliers based on conservative visual inspections. In this work we exclude all points flagged as outliers and we combine all light curves from different polarised arrays that are observed at the same frequency (e.g., PA3–f090, PA5–f090 and PA6–f090).

Ma et al. will provide a detailed uncertainty analysis of the calibration, but preliminary studies of the variance of Uranus measurements over time, as well as comparison of flux densities of the AGN between array-bands (e.g., PA5–f090 vs. PA6–f090), indicate an uncertainty of ~ 2 to 7% , depending on the array-frequency channel (c.f., Hervías-Caimapo et al. 2024). These systematic measurement errors, which are not Gaussian-distributed, cause point-to-point scatter in the light curves that is mixed in with any intrinsic variability of observed sources. However, the re-

sults of this paper do not rely on detailed knowledge of these sources of uncertainty.

2.2. Ancillary Data

Our analysis includes the following light curves from other observatories that overlap in time with the ACT light curves:

- OVRO light curves of PKS 2131–021 and PKS J0805–0111 at 15 GHz (Richards et al. 2011).
- Atacama Large Millimeter Array (ALMA) light curves of PKS 2131–021 at 91.5, 103, 104, 337, 343, 344, 349 and 350 GHz, taken from the ALMA Calibrator Source Catalogue.⁵ Following K24, we combine the 103 and 104 GHz data into a single light curve and call the combination ‘103.5 GHz’. We also combine 337–350 GHz and refer to it as ‘345 GHz’.
- The Catalina Real Time Survey (CRTS; Drake et al. 2009) light curve of PKS 2131–021 in the optical V-band.
- The Zwicky Transient Facility (ZTF; Masci et al. 2019; Graham et al. 2019) light curve of PKS 2131–021 in the optical g-band.

Data from CRTS and ZTF were rebinned to a daily cadence using a weighted mean scheme. For consistency with K24, especially in our analysis of the sinusoid phase shifts (Sec. 4.1), we use the same time spans as they did: MJD 56647.1–60053.7 for the ALMA light curves, and MJD 54470.9–60175.3 for OVRO.

3. Sine-wave fits to the light curves

3.1. Method

We fitted a sine wave function to the OVRO and ACT data by maximizing the following likelihood function:

$$\ln \mathcal{L} = -\frac{1}{2} \sum_{j=1}^4 \sum_{i=1}^{N_j} \frac{(S_{ij} - \bar{S}_j - A_j \sin[\frac{2\pi}{P}(t_{ij} - t_0) - \phi_j])^2}{\sigma_{ij}^2 + \xi_j^2} - \frac{1}{2} \sum_{j=1}^4 \sum_{i=1}^{N_j} \ln(\sigma_{ij}^2 + \xi_j^2), \quad (1)$$

where the i is the time index of the light curve and j stands for each of the light curves: OVRO 15 GHz, ACT 95 GHz, ACT 147 GHz and ACT 225 GHz, respectively. The light curves, S_{ij} , which have N_j points and uncertainties σ_{ij} , are sampled at times t_{ij} ; the reference time for the sinusoid phase is set at $t_0 = \text{MJD } 59\,000$ (2020 May 31). The period, P , is held fixed during the fit (see below), and there are four free parameters per light curve: the sine-wave offset \bar{S}_j , amplitude A_j , and phase ϕ_j , plus a term quantifying the correlated noise in the data, ξ_j .

We determine the period P by fitting the OVRO data alone in the range where there are ACT data. Then, keeping this period fixed, we do the joint fit of Eq. 1 described above. The reason for calculating the period from only in the ~ 6 -year time range where there are ACT data, rather than over the whole range of the OVRO data, is that real

² For f150 we have given the mean excluding PA1, since that array was removed before the light curves in this paper begin. With PA1 included the mean band centre of f150 is 146.9 GHz.

³ The 147 GHz data from PA4 are lacking the final, *Planck*-based correction due to issues with the ACT power spectra for these data (Naess et al. 2025). Since these corrections for other frequency-arrays are on the order of a few percent, comparable to our uncertainty (see below), this should not noticeably affect our results in this paper.

⁴ For details, see the documentation for the `matched_filter_constcorr_dual()` method in the `pixell` package: <https://github.com/simonsobs/pixell>.

⁵ <https://almascience.eso.org/alma-data/calibrator-catalogue>

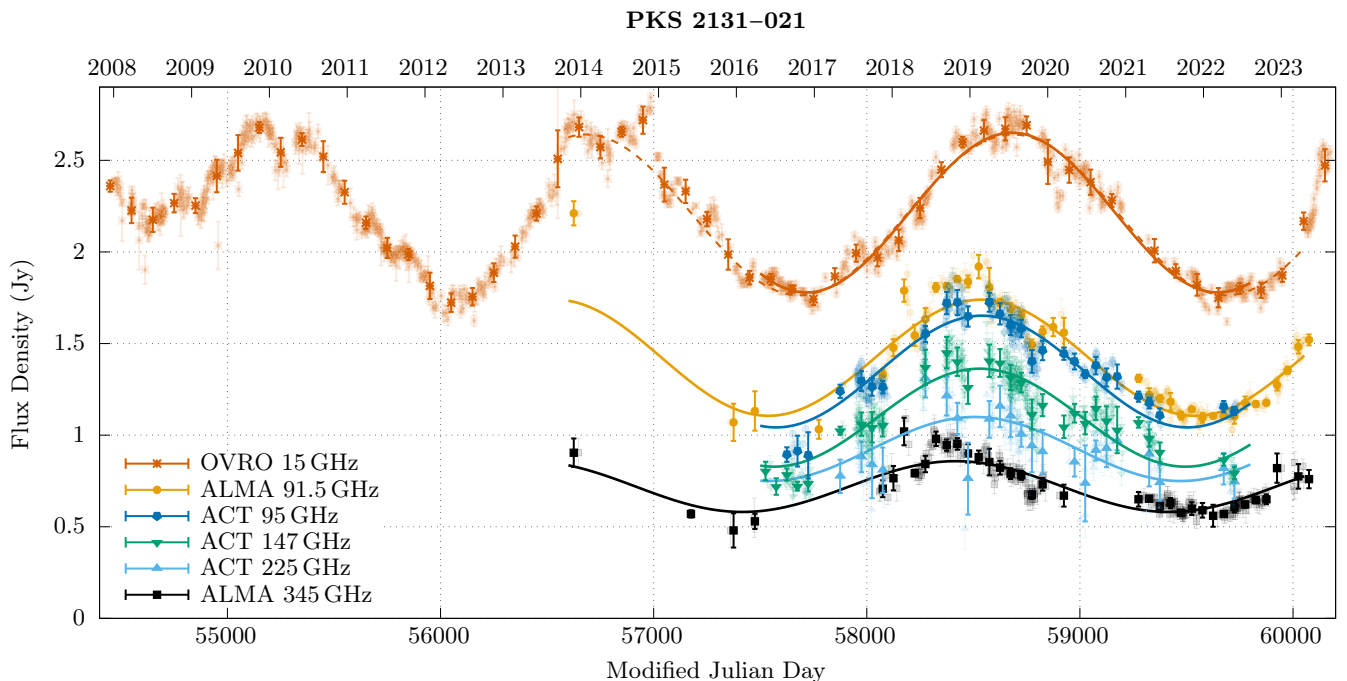


Fig. 1. PKS 2131–021 light curves from OVRO, ACT and ALMA. Heavy points are binned into 50-day intervals (100 for OVRO) to guide the eye, with individual measurements shown in lighter points. Sinusoidal fits, shown with the continuous curves, were done on the unbinned data. The sine fits for ALMA are from K24 and sine fits to ACT are done in this paper (see text). For the OVRO data, the solid curve is the best-fit for the ACT time range, while the dashed sine curve corresponds to the ALMA time range. A monotonic phase shift of the sine waves to earlier times with increasing frequency is visible by eye, and is reported relative to the OVRO phase as $\Delta\phi_0$ in Tables 1 and A.1.

Table 1. Sine-wave fit results for PKS 2131–021.

Parameter	OVRO 15 GHz	ACT 95 GHz	ACT 147 GHz	ACT 225 GHz
P (days)		1931 \pm 19 (fixed)		
A (Jy)	0.4358 \pm 0.0052	0.3048 \pm 0.0090	0.2674 \pm 0.0075	0.175 \pm 0.022
ϕ_0 (rad)	3.678 \pm 0.015	3.214 \pm 0.027	3.182 \pm 0.026	3.11 \pm 0.11
\bar{S} (Jy)	2.2148 \pm 0.0041	1.3472 \pm 0.0063	1.0954 \pm 0.0052	0.924 \pm 0.015
ξ (Jy)	0.0656 \pm 0.0032	0.0889 \pm 0.0044	0.0940 \pm 0.0039	0.125 \pm 0.014
$\Delta\phi_0$ (cycles)	0	-0.0738 \pm 0.0049	-0.0788 \pm 0.0048	-0.091 \pm 0.018
$\Delta\phi_0$ (days)	0	-142.5 \pm 9.4	-152.2 \pm 9.2	-175 \pm 35

Notes. The period, P , was determined from an initial fit including only the OVRO data in the range $57500 < \text{MJD} < 59800$. The joint fit including OVRO and the three ACT light curves kept the period fixed at this best fitting value. The fit uncertainties do not account for systematics due to superimposed, shorter term variations (see Appendix B). The reference time for the phase, in MJD, is $t_0 = 59000$. The phase shift, $\Delta\phi_0$, is defined in Eq. 2. Here, and in Tables 2 and A.1, two significant figures are retained in the quoted uncertainties for consistency across all fits and as useful for error propagation, but we do not claim to know errors to that precision (see Appendix B.1).

flux fluctuations due to processes inside the jet, which are superimposed on the sinusoidal signal, act as a source of ‘noise’ in the sine-wave fits that may not be fully captured by the correlated noise term ξ , and would require more SMBHB candidates to be properly understood. See O22, K24 and Appendix B.1 for a more detailed discussion of this source of uncertainty. Restricting the fit to the time range when both OVRO and ACT data exist is the best approach for measuring the phase shifts as a function of frequency (see Sec. 4.1, below). A result of this restriction of the time range is that the fits with ACT and ALMA data have slightly different fixed periods ($\approx 4\%$), since their time spans are not equivalent (see Fig. 1 and compare Tables 1 and A.1).

The best-fitting parameters and their uncertainties are calculated with a Markov chain Monte Carlo (MCMC) using the EMCEE code (Foreman-Mackey et al. 2013a). The phase shifts are calculated from the best-fitting values as:

$$\Delta\phi_j = (\phi_j - \phi_{\text{OVRO}})/2\pi. \quad (2)$$

The uncertainties represent the 68% confidence range of the marginalized posterior distributions. The results of the fits are reported in Tables 1 and 2; the fits to the OVRO+ALMA data, which are the same as those presented in K24 and were performed with the same methodology described above, are given in Table A.1.

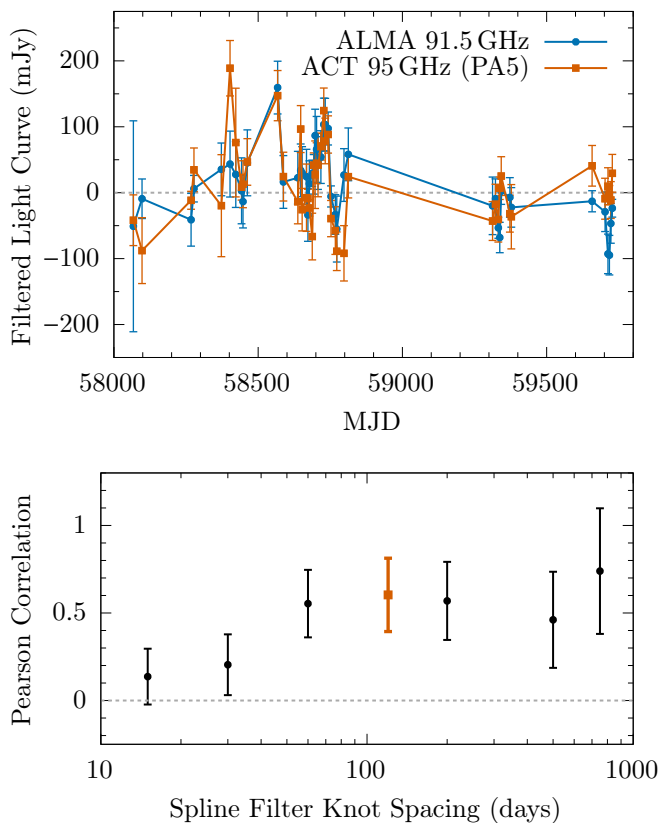


Fig. 2. Correlation of medium-term flux density variations in ALMA and ACT light curves of PKS 2131–021. *Top:* ALMA 91.5 GHz and ACT 95 GHz (PA5) light curves, which have been filtered by binning and subtracting a long timescale trend. The binning is in five day chunks, and only time chunks containing data from both ALMA and ACT are retained. The long timescale trend is removed by fitting a third degree B-spline with 120-day knot spacing to each binned light curve and subtracting; this effectively acts as a high pass filter of variations on timescales $\gtrsim 120$ days, removing the large sinusoidal pattern. Clear correlations between the light curves are seen on these time scales. *Bottom:* The Pearson correlation between the filtered ALMA and ACT light curves, for different spline knot spacings. Errors are estimated by calculating the correlations between the ALMA PKS 2131–021 light curve and each of the other 204 ACT light curves in our bright AGN library, which should be uncorrelated, and taking the standard deviation. The thick, coloured point at 120 days corresponds to the data shown in the upper panel.

3.2. The light curves of PKS 2131–021

It is fortunate that PKS 2131–021⁶ is an ALMA calibrator that was observed during the same time period as the ACT data, as it affords us the opportunity to compare the ACT 95 GHz light curve with ALMA at 91.5 and 103.5 GHz, providing a useful cross-check of the calibration of the ACT data. The ACT light curves of PKS 2131–021 at 95, 147 and 225 GHz are shown in Fig. 1, together with the OVRO 15 GHz and ALMA 91.5 GHz and 345 GHz light curves.

The ACT 95 GHz data show good consistency with the ALMA 91.5 GHz and 103.5 GHz data. We determine this

⁶ This AGN is well known in the literature as PKS J2134–0153, but we use the identifier PKS 2131–021 to be in continuity with O22 and K24.

by comparing the ratio of their light curves after colour-correcting the ALMA data to the ACT band centre using a spectral index of -0.38 ± 0.12 , which we obtained from the ratio of the ALMA 91.5 GHz and 103.5 GHz data for the 219 instances where both bands had simultaneous measurements.⁷ The mean ratio of the 95 GHz ACT flux to the 91.5 ALMA flux, using the 30 pairs of data points measured on the same day in both experiments, is 0.97 ± 0.04 . For ACT 95 GHz and ALMA 103.5 GHz, the mean ratio is 0.97 ± 0.05 , using the 28 available pairs of data. Another comparison, albeit less precise, can be made using the ratio of the best-fitting sinusoid offsets, \bar{S}_j . After colour correcting these offsets, we find: 0.96 ± 0.11 for ACT 95 GHz vs. ALMA 91.5 GHz, and 0.97 ± 0.13 for ACT 95 GHz vs. ALMA 103.5 GHz. (Note that the uncertainties here are dominated by the uncertainty in colour correction.) Farren et al. (2021) also found consistency between ACT and ALMA flux densities using a few dozen point sources. In their case, the comparison was between ACT fluxes averaged over a year and ALMA data from the same year, rather than between individual points in light curves as we have done here, which they note increases the measurement uncertainty.

A further agreement between ACT and ALMA is found in the scatter in their light curves, which is similar between the two datasets on \sim month-long time scales. This ‘scatter’ is actually due to real flux density variations in the source. We illustrate this in the top panel of Fig. 2, in which the long term sinusoidal variation of the ALMA and ACT light curves has been filtered out and the two resulting light curves exhibit similar residuals. The bottom panel shows the Pearson correlation between the ALMA 91.5 GHz and ACT 95 GHz data as a function of how aggressive this high pass filter is. On timescales > 1 month the level of correlation is significant; on shorter time scales the correlation is noise dominated.

In Fig. 1 we see a monotonic progression of the phases of the fitted sine waves with observing frequency, with the higher frequencies leading the lower frequencies. This phenomenon was discovered by K24. We analyse the phase shifts later, in Sec. 4.1.

3.3. The ACT light curve of PKS J0805–0111

We now turn to the case of PKS J0805–0111, for which there are no ALMA data. This is the second OVRO blazar discovered to exhibit significant sinusoidal variations, thereby making it a strong SMBHB candidate (D24). Best-fitting sinusoids to the ACT and OVRO data are reported in Table 2 and are shown along with the light curves in Fig. 3. The sinusoidal variation discovered at 15 GHz in the OVRO light curve of PKS J0805–0111, which lasted from 2008 to 2020 (D24), is clearly also seen in the ACT light curves, and shows that the broadband sinusoidal variation seen in PKS 2131–021 is not simply an isolated case. It suggests that broadband sinusoidal emission is a common phenomenon in SMBHB blazar candidates. The KO model explains this phenomenology which has now been confirmed

⁷ In principle, the ACT band centre should also be colour-corrected, since we have adopted the band centre for synchrotron emission, i.e., an index of -0.7 (see Sec. 2.1). However, the difference is subdominant to other uncertainties, particularly the $\approx 3\%$ scatter in band centre from detector array to detector array, and we ignore it in this analysis.

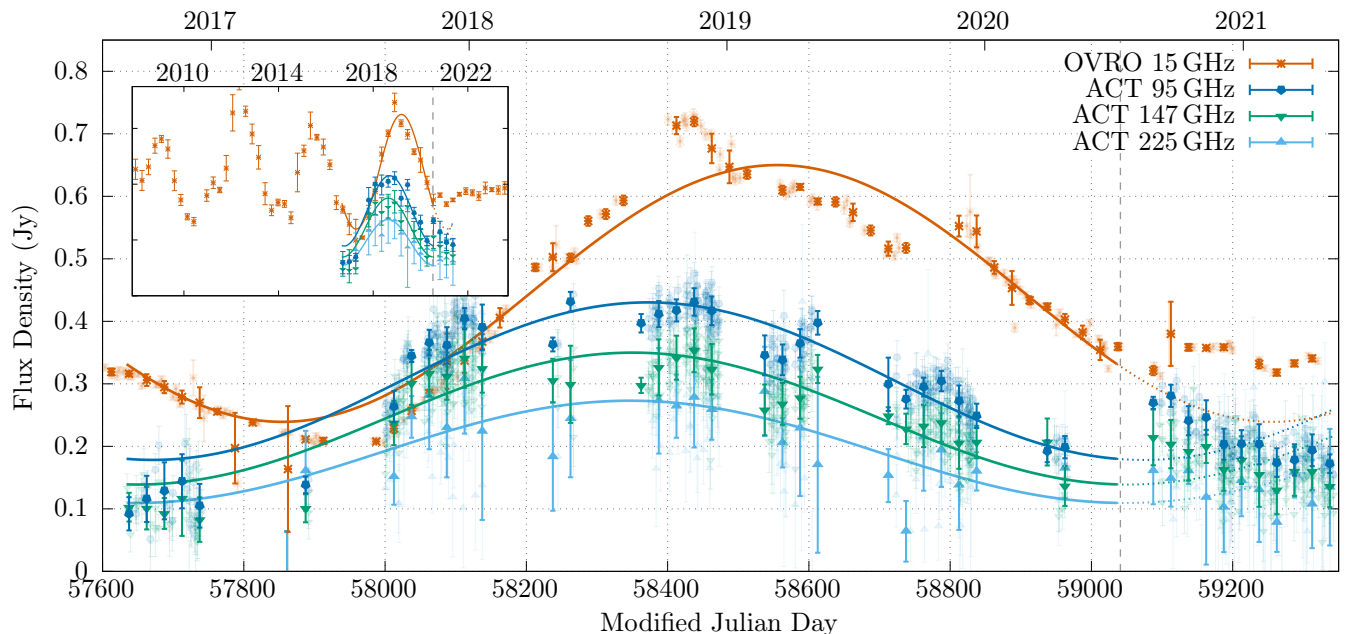
PKS J0805–0111


Fig. 3. PKS J0805–0111 light curves at 15 GHz, 95 GHz, 147 GHz, and 225 GHz. The main panel shows the time range covered by the ACT observations while the inset shows the full range observed by OVRO. Heavy points are binned into 25-day intervals (100 days in the inset) to guide the eye, with individual measurements shown in lighter points; the sinusoidal, least-squares fits were done on the unbinned data. A monotonic phase shift of the sine waves to earlier times with increasing frequency is visible by eye, and is reported relative to the OVRO phase as $\Delta\phi_0$ in Table 2. The dashed vertical line at MJD 59041 (2020 July 11) indicates the approximate date at which D24 found that the sinusoidal variation in the 15 GHz ceases. The ACT mm data also apparently flatten around the same time.

Table 2. Sine-wave fit results for PKS J0805–0111.

Parameter	OVRO 15 GHz	ACT 95 GHz	ACT 147 GHz	ACT 225 GHz
P (days)		1402 \pm 23 (fixed)		
A (Jy)	0.2054 \pm 0.0057	0.1260 \pm 0.0031	0.1055 \pm 0.0029	0.0818 \pm 0.0087
ϕ_0 (rad)	2.721 \pm 0.028	1.899 \pm 0.022	1.803 \pm 0.024	1.786 \pm 0.090
\bar{S} (Jy)	0.4446 \pm 0.0040	0.3043 \pm 0.0021	0.2444 \pm 0.0019	0.1912 \pm 0.0054
ξ (Jy)	0.0482 \pm 0.0030	0.0386 \pm 0.0017	0.0375 \pm 0.0017	0.0342 \pm 0.0084
$\Delta\phi_0$ (cycles)	0.0	-0.1307 \pm 0.0057	-0.1461 \pm 0.0058	-0.1488 \pm 0.0150
$\Delta\phi_0$ (days)	0.0	-183.3 \pm 7.9	-204.8 \pm 8.2	-209 \pm 21

Notes. The period, P , was determined from an initial fit including only the OVRO data in the range $57634 < \text{MJD} < 59343$. The joint fit including OVRO and the three ACT light curves kept the period fixed at this best fitting value. The fit uncertainties do not account for systematics due to superimposed, shorter term variations (see Appendix B.1). The reference time for the phase, in MJD, is $t_0 = 59000$. The phase shift, $\Delta\phi_0$, is defined in Eq. 2.

in our two, high significance SMBHB candidates. This could be important for the detection of GW from SMBHBs.

D24 found that the sinusoidal variations in the 15 GHz OVRO light curve ceased at around MJD 59041, shown in Fig. 3 with a dashed, vertical line. Although the ACT light curves do not extend long after this date, they too appear consistent with the sinusoid shutting off. A similar phenomenon was also observed by O22 and K24 in PKS 2131–021 in more than 45 years of data: its light curve was sinusoidal for about the first seven years, then non-sinusoidal for about 20 years, after which the sinusoid recommenced with a smaller amplitude but in phase with the original sine wave and with a similar period. This suggests that the underlying mechanism producing the sinusoid, i.e., the SMBHB orbit, persisted when the light curve

became quiescent. Such behaviour is not explained by KO model *per se*, but O22 and K24 point out that the disappearance of the sinusoid, as well as the change in its amplitude when it reappears, could plausibly be produced by changes in the fuelling of the jet.

As in the case of PKS 2131–021, a monotonic phase shift with frequency is observed in the light curves, which we analyse in Sec. 4.1, below.

4. Multi-frequency properties of the SMBHB candidates

4.1. Frequency-dependent phase shifts

As noted in the previous section, in both of our sources the higher frequency ACT light curves are shifted towards

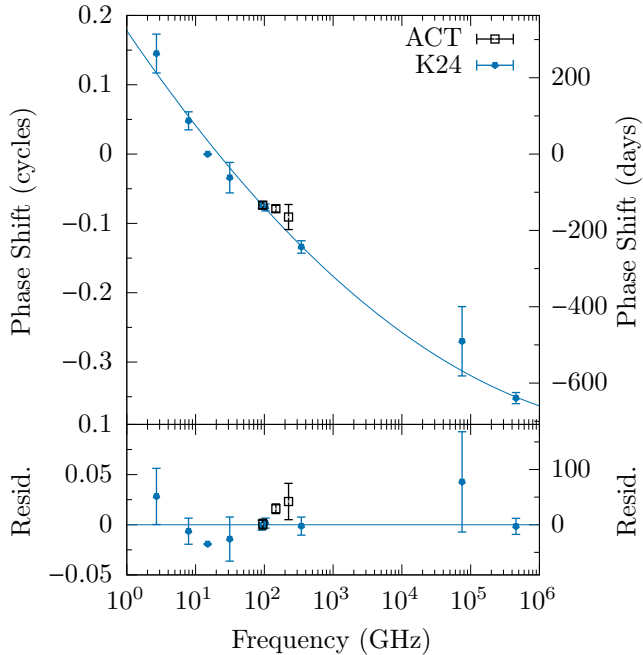


Fig. 4. PKS 2131–021 phase shifts measured by ACT at 95 GHz, 147 GHz, and 225 GHz (black points), compared to the phase shift results of K24 (blue points); see Table 3. Note that the ACT 95 GHz and ALMA 91.5 GHz points overlap. The Haystack or OVRO 15 GHz light curves provided the phase reference in all cases. Uncertainties are determined by the MCMC sine-wave fits (Eq. 1). The curved line shows the quadratic fit determined by K24 (Eq. 3).

earlier times relative to the OVRO 15 GHz light curves, and the shift is monotonic with frequency. This behaviour is explained by the KO model as being due to frequencies originating at different positions along the jet because of optical depth effects (see Sec. 1).

Table 3 shows the phase shifts for PKS 2131–021. In addition to the phase shifts of the ACT light curves relative to OVRO, it includes the phase shifts of light curves from the Haystack observatory (radio), ALMA (mm), the Wide-field Infrared Survey Explorer (WISE; infrared) and ZTF (optical), all relative to OVRO, as listed in table 2 of K24. Note that the Haystack data came from an earlier time period (1975–1983) and did not overlap with the other datasets; thus, the phase shift for the Haystack light curves are relative to the 15.5 GHz Haystack channel. The coherent behaviour from 2.7 GHz to optical wavelengths is strikingly illustrated by Fig. 4, which shows the phase shift measurements on top of the best-fit quadratic phase–frequency relation from K24,

$$\Delta\phi = 0.178 - 0.146 \log_{10}(\nu) + 0.0093[\log_{10}(\nu)]^2. \quad (3)$$

The ACT 95 GHz measurement agrees with this curve, and is consistent with the ALMA measurement, while the 147 GHz measurement is 3.3σ higher than the curve; the 225 GHz measurement is also higher, but only by 1.3σ . We discuss these deviations below.

Table 4 lists the phase shifts for PKS J0805–0111. Note that, as found in PKS 2131–021, the ACT sinusoids are shifted towards earlier times relative to the OVRO 15 GHz light curve, and the shift is consistent with being monotonic with frequency. This is therefore likely to be a common phe-

Table 3. PKS 2131–021 Phase Shifts with Frequency

Instrument	Frequency Band	Phase (Fraction of cycle)	Uncert. (Fraction of cycle)
Haystack	2.7 GHz	0.145	0.028
Haystack	7.9 GHz	0.048	0.013
Haystack/OVRO	15 GHz ^a	0	0
Haystack	31.4 GHz	−0.034	0.022
ALMA	91.5 GHz	−0.073	0.005
ACT	95 GHz	−0.074	0.005
ALMA	103.5 GHz	−0.077	0.005
ACT	147 GHz	−0.079	0.005
ACT	225 GHz	−0.091	0.018
ALMA	345 GHz	−0.134	0.009
WISE	infrared ^b	−0.27	0.05
ZTF	optical ^c	−0.352	0.008

Notes. The OVRO light curve was the phase reference, except for the Haystack data, whose light curves do not overlap with the others, and which use the Haystack 15.5 GHz channel as the reference. Apart from the ACT results, data in this table are taken directly from table 2 of K24.

(^a) The Haystack channel is 15.5 GHz; OVRO is 15 GHz. (^b) Both the WISE 1 (2.8–3.8 μm) and WISE 2 (4.1–5.2 μm) bands were analysed, and gave the same phase shift. (^c) ZTF phase shift is from the combined r -, g - and i -bands.

Table 4. PKS J0805–0111 Phase Shifts with Frequency Relative to the 15 GHz Light Curve

Frequency Band	Phase (Fraction of cycle)	Uncertainty (Fraction of cycle)
15 GHz	0	0
95 GHz	−0.131	0.006
147 GHz	−0.146	0.006
225 GHz	−0.149	0.015

Notes. The 15 GHz light curve was used as the phase reference for the ACT data.

nomenology in SMBHB blazar candidates and a signature of a fundamental property of these jets.

The exact form of the frequency phase–shift relation depends on the details of where different frequencies originate in the blazar jet. The simple quadratic fit of Eq. 3, shown in Fig. 4, is not motivated by any particular jet model but is purely phenomenological. As noted above, it does not agree well with the ACT data, which exhibit a shallower slope in the range 95–225 GHz. This frequency range coincides with a steepening of the blazar’s spectrum in the range ~ 70 –353 GHz identified by K24 (see their figure 4), which they suggest could be caused by the mm coming from an optically thin zone in the jet. In the frequency–phase relation shown in Fig. 1, it can also be observed that at the low frequencies, 2.7–31.4 GHz, the slope is steeper than the phenomenological quadratic fit. It is entirely possible that these features in the slope of the frequency–phase relation are real and constitute an important property of the jet, which could be optically thicker in the radio regime and then become optically thinner in the mm. It is further possible that changes in the jet properties cause the frequency–phase relation to be time-variable. Indeed, the steepening of

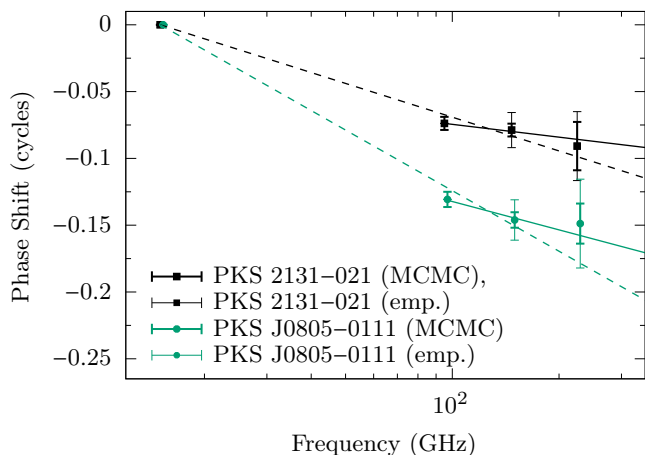


Fig. 5. Phase shifts of the ACT best-fit sinusoids relative to the OVRO 15 GHz light curves for each of PKS 2131–021 and PKS J0805–0111. The dashed (solid) lines show the best-fit slope from 15 GHz to 225 GHz (95 GHz to 225 GHz); Table 5 lists the slopes. Heavy errorbars are the fiducial uncertainties of the phase shifts from the MCMC fits (Sec. 3.1) relative to 15 GHz, while the light errorbars show an empirically-derived, relative phase uncertainty between 95 GHz and 147/225 GHz (see Appendix B.1). Fits are done with the fiducial uncertainties.

the blazar’s spectrum reported by K24, referred to above, is time dependent. Their result is derived from fluxes in nine bands between 30 and 857 GHz from the *Planck* satellite, measured during seven epochs spanning a total of 3.5 years. The spectral steepening ends anywhere from ~ 217 GHz to ~ 545 GHz, depending on the epoch, and is thus time variable. If both the spectral steepening, shown in K24, and the flattening of the frequency–phase shift relation, shown in Fig. 4, are due to the same jet property, then one might expect that phase shift in the ALMA 353 GHz band, which in Fig. 4 does not appear to share the flattening seen at 95–225 GHz, could become flattened in other epochs.

Fig. 5 compares the frequency–phase relations of PKS 2131–021 and PKS J0805–0111. The PKS J0805–0111 data also exhibit a flatter slope in the mm regime compared to the slope extending to the 15 GHz OVRO point, suggesting that this may be a property common to SMBHB jets. To quantify this, we have fitted two slopes for each of our SMBHB candidates: first, we fitted the slope of the 95, 147 and 225 GHz phase shifts relative to 15 GHz; second, we fitted the slope of the 147 and 225 GHz phase shifts relative to 95 GHz. The slopes are shown in Fig. 5 and listed in Table 5. Two points should be noted:

1. For both SMBHB candidates, the phase shift between 15 GHz and 95, 147 and 225 GHz is highly significant: χ^2 for the null hypothesis of no phase shift is 522 and 1259, with three degrees of freedom, for PKS 2131–021 and PKS J0805–0111, respectively. Thus, regardless of the details of how the slope behaves in the mm regime (point 2, below), the ACT data provide a strong detection of the phase shift between the radio and mm sinusoidal emission.
2. The slope is $\sim 2\times$ shallower in the 95–225 GHz regime for both SMBHB candidates (see the ‘Ratio’ column in Table 5). However, particularly in the case of PKS 2131–021 the uncertainty on this ratio is too large

Table 5. Slope of the $\log_{10}(\nu)$ –phase relation.

AGN	Slope ($100 \times \text{cycle} / \log(\nu)$) ^a		Ratio
	15–225 GHz	95–225 GHz	
PKS 2131	-8.4 ± 0.4	-3.2 ± 2.7	2.6 ± 2.2
PKS J0805	-15.1 ± 0.4	-7.1 ± 2.2	2.1 ± 0.7

Notes. The 15–225 GHz range fits the 95, 147 and 225 GHz phase shifts relative to 15 GHz. The 95–225 GHz fits the 147 and 225 GHz phase shifts relative to 95 GHz. The MCMC uncertainties (Sec. 3.1) been used in these fits.

^(a) The slope is in percentage of a cycle (i.e., $100 \times \text{cycle}$) per $\log \nu$ where ν is in GHz.

to draw any firm conclusions. More mm data for these and, ideally, additional SMBHB candidates, together with more precise estimates of the uncertainties (see below) would elucidate if we have discovered a feature that is general to SMBHB jets.

Improving on these results above would benefit not only from more data, but would also require better understanding of the uncertainties of the phase shifts. As discussed in K24, intrinsic variations in the jet that are superimposed on the sinusoidal variations can add covariance between the light curves at different frequencies, complicating the noise model used in fitting. We discuss this further in Appendix B, where we also make an empirical estimate of the phase shift uncertainties by injecting sine waves into other, real ACT light curves. These uncertainties are shown with light errorbars in Fig. 5. Our analysis suggests that the MCMC-derived errorbars listed in Tables 1 and 2 and shown with heavy errorbars in Fig. 5, are possibly underestimated. However, as we argue in Appendix B, light curves of more SMBHB candidates are needed to make such an assessment. Within the scope of this paper, our main findings in this section are unaffected by the exact size of the uncertainties: in both PKS 2131–021 and PKS J0805–0111, the phase shift is monotonic and exhibits a possible flattening in slope in the mm regime.

4.2. Achromatic variability

Both the sinusoidal variation in emission (Sec. 3) and the frequency-dependent phase shifts just discussed (Sec. 4.1) provide important constraints on the physical origin of the emission and are predicted by the KO model. The model also predicts that the fractional amplitude of the sinusoidal variations should be achromatic, which is a third feature we verify in our data. The fractional change in intensity, expressed as A/\bar{S} , is similar for all frequencies (see Tables 1 and 2). K24 noted that it only varied by a factor of ~ 2 – 3 over five decades in frequency, though their picture is complicated somewhat by the fact that the data were taken at several epochs. In contrast, K24 show that the OVRO and ALMA data, which were contemporaneous, show remarkably achromatic behaviour. In the OVRO+ACT data at 15, 95, 147 and 225 GHz, we find $A/\bar{S} = (21.4 \pm 2.2)\%$ for PKS 2131–021, where the quoted uncertainty is the standard deviation of the four frequencies, and $(43.4 \pm 1.7)\%$ for PKS J0805–0111.

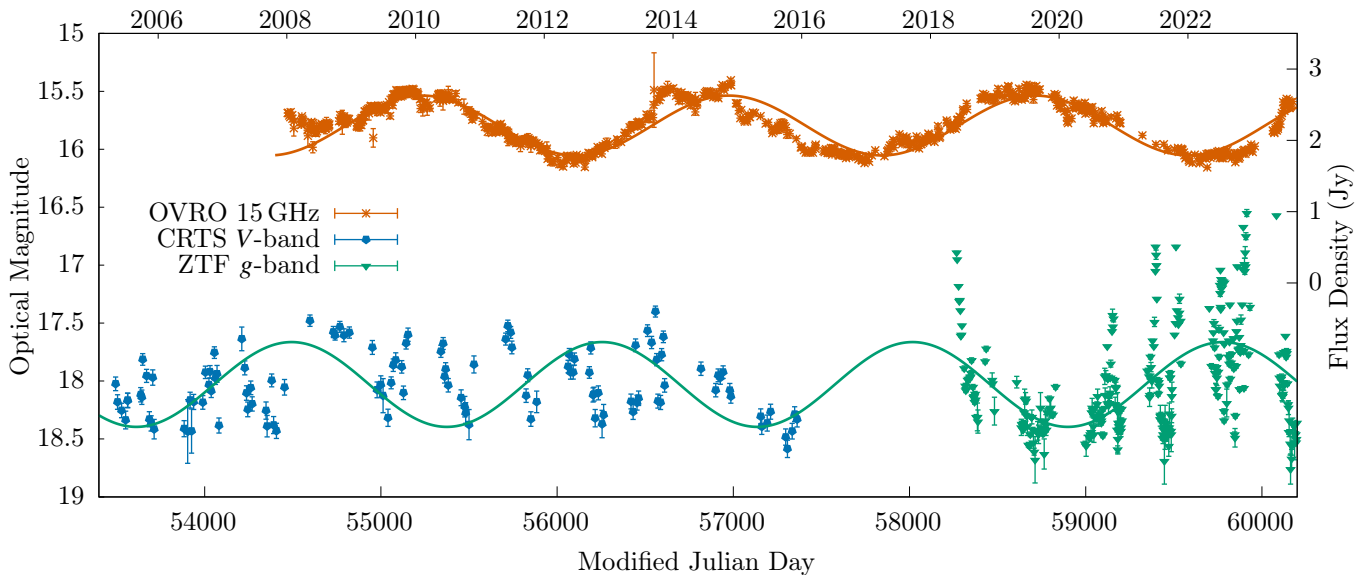


Fig. 6. Comparison of radio and optical light curves of PKS 2131–021. The sine waves shown in the figure come from tables 1 and 4 of K24 for the radio and ZTF optical data, respectively.

5. The value of millimetre light curves for SMBHB searches

A notable feature of the mm light curves shown in Figs. 1 and 3 is their short-term deviations from the sinusoids. However, for the 95 and 147 GHz light curves, the sinusoidal variation dominates by a factor of ~ 2 – 3 (see the SNR_{sin} values in Table B.2). Thus, although the mm light curves do not have the same sensitivity as the OVRO 15 GHz light curves, and hence the uncertainties on individual observations are much larger in the ACT than in the OVRO data, this does not mean that ACT is less able to pick out sinusoidal light curves in blazars than the OVRO, provided we consider equal timespans.⁸ This argues *strongly* for continued, long term observations with mm survey instruments, such as the South Pole Telescope (Carlstrom et al. 2011; Benson et al. 2014) and the Simons Observatory (SO; Ade et al. 2019; Abitbol et al. 2025) for multi-messenger astronomy.

The promise of cm, mm, and submm data for identifying and studying SMBHB is evident when they are placed side by side with optical data. Fig. 6 shows the OVRO 15 GHz light curve of PKS 2131–021 together with optical light curves of the same object from the Catalina Real Time Survey (CRTS; Drake et al. 2009) and Zwicky Transient Facility (ZTF; Masci et al. 2019; Graham et al. 2019). In Appendix C we give a detailed account of the statistical tests we have carried out on the CRTS and ZTF data for PKS 2131–021. These show that the optical data alone do not provide compelling evidence for the periodicity we see in PKS 2131–021, unless they are sampled about 3 times a week and then averaged for a long period (\sim several months) to eliminate the rapid large fluctuations at optical wavelengths. The cm, mm, and submm observations also have

the great advantage that they can be sampled year-round, while at optical frequencies the daylight sky is bright compared to even the brightest optical blazar, 3C 273, which has an apparent optical magnitude of $V \sim 13$,⁹ so year-round optical monitoring of blazars is not possible.¹⁰

As discussed in K24, the ZTF data show much stronger short-term variations than the radio–submm data, but when averaged over a year they follow a sine wave well and have a period consistent with that derived from the OVRO and Haystack 15 GHz observations. In Fig. 6 the sine wave fitted to the ZTF data by K24 (reported in their table 4) has been extrapolated back to the period covered by the CRTS. There is no clear correspondence between the curve and the CRTS data points. This shows that searches for SMBHB candidates similar to PKS 2131–021 are unlikely to be found in the CRTS because the cadence is not frequent enough. The ZTF cadence is two days, and that clearly works well, although the short-term variations are much greater than at cm–mm–submm wavelengths. However, there may well be other types of SMBHB candidates that show more prominent sinusoidal variations at optical wavelengths. PG 1302–102 might be just such an example (Graham et al. 2015); this source also shows radio periodicity at the same period as detected in the optical (Qian et al. 2018).

6. Discussion and conclusions

ACT mm data at 95, 147 and 225 GHz have confirmed the presence of a sinusoidal variation in the light curves of PKS 2131–021 and PKS J0805–0111 that had been detected with high significance in OVRO 15 GHz data by O22, D24 and K24. Our results demonstrate the value of high ca-

⁸ The 225 GHz channel has more noise due to the larger atmospheric contamination it suffers, and also has lower fluxes due to the falling synchrotron spectrum. It will therefore not be as important a channel for SMBHB detection. Nonetheless, for our SMBHB candidates, its SNR of ≈ 1 (Table B.2), will still allow 225 GHz data to be used to study phase shifts and spectra.

⁹ See the NASA/IPAC Extragalactic Database (NED).

¹⁰ While AGN can be observed in daylight in the mm, it is still the case that mid-latitude CMB surveys will have observing gaps for most AGNs for part of the year—about one month for SO—due to Sun- and Moon-avoidance in their observation strategies (Abitbol et al. 2025).

dence, wide area surveys of the mm and submm sky available from present and future CMB experiments.

Our main findings are as follows:

1. The ACT 95 GHz light curve of PKS 2131–021 is in good agreement with the ALMA 91.5 and 103.5 GHz light curves, including in their small variations superimposed on the larger sinusoid variation. This confirms that the ACT calibration and data reduction of light curves are working well.
2. ACT light curves of PKS J0805–0111, for which no ALMA data are available, corroborate the finding in D24 that this source is a SMBHB candidate. Especially compelling is the fact that the sinusoid appears to turn off in the ACT light curves in the same manner as in the OVRO data in mid-2020 (see Fig. 3). This provides further evidence that: (a) the long time-scale variations of the mm light curves are tracing the same underlying physics as the radio light curve and (b) that the phenomenon of the sinusoid stopping and starting, discovered in O22 for PKS 2131–021, is likely a common feature of SMBHB candidates. O22 demonstrated that when the sinusoid restarted in 2003 after a 19 year hiatus, it returned not only with the same period, but also in phase with the original curve, so it is likely that the underlying periodic behaviour continued during the gap. Further data will help clarify the physical origin of the intermittency, and our results show that mm observations can play a key role in detecting this behaviour.
3. The ACT data confirm that the sinusoidal variations at higher frequencies are shifted in phase relative to radio frequencies, a feature that is naturally explained in the KO model by light-travel times due to higher frequencies originating from deeper in the jet. In both cases the mm phase leads the radio phase in time.
4. The ACT data from 95 GHz to 225 GHz show a smaller change in phase as a function in frequency – a flattening – compared to other regimes of the electromagnetic spectrum probed to date. This could be due to an optically thinner zone that also causes the spectral steepening in a similar frequency range reported by K24. However, the current uncertainties on the phase shifts from ACT do not allow us to make a definite claim about this. Within the errorbars, the ACT phase shifts in PKS 2131–021 are consistent with a single, linear slope in log-frequency from 15 to 225 GHz, while the phase shifts for PKS J0805–0111 show $\approx 3\sigma$ evidence for a shallower slope from 95 to 225 GHz.
5. The sinusoidal signal is achromatic from 15 to 225 GHz, i.e., the ratio of its amplitude to offset, A/\bar{S} , is nearly constant at all measured frequencies in this range. This is expected under the KO model and is further evidence for these objects being SMBHBs.
6. In PKS 2131–021, the ratio of the sinusoid amplitude to the non-sinusoidal variations in the mm data is significantly higher than in optical data, which are contaminated by large, short term variability from the point of view of detecting SMBHB candidates. It is possible that some SMBHB candidates will appear more cleanly in the optical (e.g., PG 1302–102), but our findings provide motivation for using mm surveys to search for SMBHB. Such searches will be complementary to radio, submm and optical searches.

The large aperture telescope (LAT) of SO will observe 25 000 deg² of the sky from 2025 to 2034 at 27, 39, 93, 145, 225 and 280 GHz with a planned cadence of 1–2 days (Abitbol et al. 2025).¹¹ We use their goal sensitivity for single observations at 93 GHz to forecast the number of AGN that SO can monitor over a 21 000 deg² sky area (to exclude the Galactic plane), using the 90 GHz radio number counts of Lagache et al. (2020). We find that SO will be able to monitor ~ 8000 AGN with a signal-to-noise > 5 , if we allow six measurements to be binned together (i.e., corresponding to a 1–2 week cadence). The number will increase to ~ 12000 when the Advanced SO upgrades, which will double the number of detectors, are completed in 2028. K24 and D24 estimate that ~ 1 in 100 blazars is an SMBHB candidate. If this is correct then SO should be able to observe $\mathcal{O}(100)$ SMBHB candidates. We anticipate, therefore, that the SO will open up a new window on SMBHB. At this point PKS 2131–021 is the only blazar in which sinusoidal variations have been observed at both optical and radio wavelengths, but this is unlikely to be an isolated case given the broadband sinusoidal variations of PKS J0805–0111 that we present in this paper. It is to be expected, therefore, that the SO will discover many SMBHB candidates.

Acknowledgements

This work was supported by the U.S. National Science Foundation through awards AST-0408698, AST-0965625, and AST-1440226 for the ACT project, as well as awards PHY-0355328, PHY-0855887, and PHY-1214379. Funding was also provided by Princeton University, the University of Pennsylvania, and a Canada Foundation for Innovation (CFI) award to UBC.

ACT operated in the Parque Astronómico Atacama in northern Chile under the auspices of the Agencia Nacional de Investigación y Desarrollo (ANID; formerly Comisión Nacional de Investigación Científica y Tecnológica de Chile, or CONICYT). We thank the Republic of Chile for hosting ACT in the northern Atacama, and the local indigenous Licanantay communities whom we follow in observing and learning from the night sky.

The development of multichroic detectors and lenses for ACT was supported by NASA grants NNX13AE56G and NNX14AB58G. Detector research at NIST was supported by the NIST Innovations in Measurement Science program. Computing for ACT was performed using the Princeton Research Computing resources at Princeton University, the National Energy Research Scientific Computing Center (NERSC), and the Niagara supercomputer at the SciNet HPC Consortium. SciNet is funded by the CFI under the auspices of Compute Canada, the Government of Ontario, the Ontario Research Fund–Research Excellence, and the University of Toronto.

Colleagues at AstroNorte and RadioSky provided logistical support for ACT and kept operations in Chile running smoothly. We also thank the Mishrahi Fund and the Wilkinson Fund for their generous support of the project.

The OVRO programme was supported by NASA grants NNG06GG1G, NNX08AW31G, NNX11A043G, and NNX13AQ89G from 2006 to 2016 and NSF grants AST-0808050 and AST-1109911 from 2008 to 2014. This work

¹¹ Though see footnote 10.

is currently supported by NSF grants AST2407603 and AST2407604.

This is not an official SO Collaboration paper.

ADH acknowledges support from the Sutton Family Chair in Science, Christianity and Cultures, from the Faculty of Arts and Science, University of Toronto, and from the Natural Sciences and Engineering Research Council of Canada (NSERC) [RGPIN-2023-05014, DGEGR-2023-00180], and is further grateful to the Lumen Christi Institute for support that enabled a research visit to the University of Chicago, during which significant portions of this work were done. S.K. was funded by the European Union ERC-2022-STG – BOOTES – 101076343. Views and opinions expressed are however those of the author(s) only and do not necessarily reflect those of the European Union or the European Research Council Executive Agency. Neither the European Union nor the granting authority can be held responsible for them. CS acknowledges support from the Agencia Nacional de Investigación y Desarrollo (ANID) through Basal project FB210003. MJG acknowledges support from NSF grant AST-2108402.

This paper makes use of the following ALMA data: ADS/JAO.ALMA#2011.0.00001.CAL. ALMA is a partnership of ESO (representing its member states), NSF (USA) and NINS (Japan), together with NRC (Canada), NSTC and ASIAA (Taiwan), and KASI (Republic of Korea), in cooperation with the Republic of Chile. The Joint ALMA Observatory is operated by ESO, AUI/NRAO and NAOJ. The National Radio Astronomy Observatory is a facility of the National Science Foundation operated under cooperative agreement by Associated Universities, Inc.

The CSS survey is funded by the National Aeronautics and Space Administration under Grant No. NNG05GF22G issued through the Science Mission Directorate Near-Earth Objects Observations Program. The CRTS survey is supported by the U.S. National Science Foundation under grants AST-0909182 and AST-1313422.

ZTF is supported by the NSF under Grants No. AST-1440341 and AST-2034437 and a collaboration including current partners Caltech, IPAC, the Oskar Klein Center at Stockholm University, the University of Maryland, University of California, Berkeley, the University of Wisconsin at Milwaukee, University of Warwick, Ruhr University, Cornell University, Northwestern University and Drexel University. Operations are conducted by COO, IPAC, and UW.

This research has made use of the NASA/IPAC Extragalactic Database (NED), which is funded by the National Aeronautics and Space Administration and operated by the California Institute of Technology.

Some of the results/plots in this paper have been derived/produced using the following software: ASTROPY,¹² a community-developed core Python package for Astronomy (Astropy Collaboration 2013, 2018, 2022); EMCEE (Foreman-Mackey et al. 2013b); GNU PLOT;¹³ NUMPY (Harris et al. 2020); PIXELL;¹⁴ and SCIPY (Virtanen et al. 2020).

References

Abitbol, M., Abril-Cabezas, I., Adachi, S., et al. 2025, arXiv e-prints, arXiv:2503.00636

¹² <http://www.astropy.org>

¹³ <http://www.gnuplot.info/>

¹⁴ <https://github.com/simonsobs/pixell>

- Ade, P., Aguirre, J., Ahmed, Z., et al. 2019, *J. Cosmology Astropart. Phys.*, 2019, 056
- Agazie, G., Anumalapludi, A., Archibald, A. M., et al. 2023a, *ApJ*, 951, L8
- Agazie, G., Anumalapludi, A., Archibald, A. M., et al. 2023b, *ApJ*, 951, L50
- Astropy Collaboration. 2013, *A&A*, 558, A33
- Astropy Collaboration. 2018, *AJ*, 156, 123
- Astropy Collaboration. 2022, *ApJ*, 935, 167
- Backer, D. C., Kulkarni, S. R., Heiles, C., Davis, M. M., & Goss, W. M. 1982, *Nature*, 300, 615
- Benson, B. A., Ade, P. A. R., Ahmed, Z., et al. 2014, in *Society of Photo-Optical Instrumentation Engineers (SPIE) Conference Series*, Vol. 9153, *Millimeter, Submillimeter, and Far-Infrared Detectors and Instrumentation for Astronomy VII*, ed. W. S. Holland & J. Zmuidzinas, 91531P
- Blandford, R., Meier, D., & Readhead, A. 2019, *ARA&A*, 57, 467
- Carlstrom, J. E., Ade, P. A. R., Aird, K. A., et al. 2011, *PASP*, 123, 568
- Choi, S. K., Hasselfield, M., Ho, S.-P. P., et al. 2020, *J. Cosmology Astropart. Phys.*, 2020, 045
- Coulton, W., Madhavacheril, M. S., Duivenvoorden, A. J., et al. 2024, *Phys. Rev. D*, 109, 063530
- De la Parra, P. V., Kiehlmann, S., Mroz, P., et al. 2024, arXiv e-prints, arXiv:2408.02645
- Drake, A. J., Djorgovski, S. G., Mahabal, A., et al. 2009, *ApJ*, 696, 870
- Emmanoulopoulos, D., McHardy, I. M., & Papadakis, I. E. 2013, *MNRAS*, 433, 907
- EPTA Collaboration. 2023, *A&A*, 678, A50
- Farren, G. S., Partridge, B., Kneissl, R., et al. 2021, *ApJS*, 256, 19
- Foreman-Mackey, D., Hogg, D. W., Lang, D., & Goodman, J. 2013a, *PASP*, 125, 306
- Foreman-Mackey, D., Hogg, D. W., Lang, D., & Goodman, J. 2013b, *PASP*, 125, 306
- Graham, M. J., Djorgovski, S. G., Stern, D., et al. 2015, *Nature*, 518, 74
- Graham, M. J., Kulkarni, S. R., Bellm, E. C., et al. 2019, *PASP*, 131, 078001
- Harris, C. R., Millman, K. J., van der Walt, S. J., et al. 2020, *Nature*, 585, 357
- Henderson, S. W., Allison, R., Austermann, J., et al. 2016, *Journal of Low Temperature Physics*, 184, 772
- Hervias-Caimapo, C., Naess, S., Hincks, A. D., et al. 2024, *MNRAS*, 529, 3020
- Kiehlmann, S. 2023, *lcsim: Light curve simulation code*, *Astrophysics Source Code Library*, record ascl:2310.002
- Kiehlmann, S., Vergara De La Parra, P., Sullivan, A., et al. 2024, arXiv e-prints, arXiv:2407.09647
- Krolik, J. H. & Di Matteo, T. 2000, *American Journal of Physics*, 68, 489
- Lagache, G., Béthermin, M., Montier, L., Serra, P., & Tucci, M. 2020, *A&A*, 642, A232
- Lomb, N. R. 1976, *Ap&SS*, 39, 447
- Madhavacheril, M. S., Hill, J. C., Naess, S., et al. 2020, *Phys. Rev. D*, 102, 023534
- Marriage, T. A., Baptiste Juin, J., Lin, Y.-T., et al. 2011, *ApJ*, 731, 100
- Masci, F. J., Laher, R. R., Rusholme, B., et al. 2019, *PASP*, 131, 018003
- Max-Moerbeck, W., Richards, J. L., Hovatta, T., et al. 2014, *MNRAS*, 445, 437
- Miles, M. T., Shannon, R. M., Reardon, D. J., et al. 2025, *MNRAS*, 536, 1489
- Naess, S., Guan, Y., Duivenvoorden, A. J., et al. 2025, arXiv e-prints, arXiv:2503.14451
- Niemack, M. D. 2008, PhD thesis, Princeton University, New Jersey
- O'Neill, S., Kiehlmann, S., Readhead, A. C. S., et al. 2022, *ApJ*, 926, L35
- Qian, S. J., Britzen, S., Witzel, A., Krichbaum, T. P., & Kun, E. 2018, *A&A*, 615, A123
- Readhead, A. C. S. 1980, in *Objects of High Redshift*, ed. G. O. Abell & P. J. E. Peebles, Vol. 92, 165–175
- Readhead, A. C. S. 2024, *Journal of Astronomical History and Heritage*, 27, 453
- Readhead, A. C. S., Cohen, M. H., Pearson, T. J., & Wilkinson, P. N. 1978, *Nature*, 276, 768
- Readhead, A. C. S. & Hewish, A. 1974, *MmRAS*, 78, 1
- Richards, J. L., Max-Moerbeck, W., Pavlidou, V., et al. 2011, *ApJS*, 194, 29
- Scargle, J. D. 1982, *ApJ*, 263, 835
- Sobacchi, E., Sormani, M. C., & Stameria, A. 2017, *MNRAS*, 465, 161
- Swetz, D. S., Ade, P. A. R., Amiri, M., et al. 2011, *ApJS*, 194, 41
- Thornton, R. J., Ade, P. A. R., Aiola, S., et al. 2016, *ApJS*, 227, 21
- Virtanen, P., Gommers, R., Oliphant, T. E., et al. 2020, *Nature Methods*, 17, 261
- Zechmeister, M. & Kürster, M. 2009, *A&A*, 496, 577

Appendix A: ALMA sine-wave fit results

K24 performed sine-wave fits to the OVRO and ALMA data for PKS 2131–021 using the same methodology described in Sec. 3.1, but only reported the best-fitting phase shifts. For completeness we include all the best-fitting parameters from this analysis in Table A.1.

Appendix B: Empirical estimates of phase shift uncertainties

Appendix B.1: Background

Given the important information about SMBHB jet physics encoded in the phase of the sinusoidal variation of the light curves as a function of frequency, it is important to assess how well we can measure those phase shifts. There are at least two types of uncertainty associated with them. The *absolute error* encodes how uncertain the phase measurement of a light curve is with respect to the true, underlying sinusoid. The *relative error* encodes how uncertain the phase shifts at two different frequencies are with respect to each other, rather than to the true, underlying sinusoid. This is the more relevant uncertainty for probing how the location of the emission zone in the jet varies with frequency. If the light curves consisted of a pure sine wave with white noise, then the absolute and relative errors would be identical. In reality, the noise is correlated within single light curves and between light curves of different frequencies, and so the two types of uncertainty will be different.

Some background on physical origin of the light curves is in order. The radio flux density variations in blazars originate from a number of sites along the jet, but are dominated by the variations in the core, which is unresolved even by very long baseline imaging (VLBI; Blandford et al. 2019). These variations in blazars are believed to generally follow a power law spectrum (see, e.g., Max-Moerbeck et al. 2014), so it is to be expected that there will be ongoing, non-sinusoidal variations on both longer and shorter timescales than the sinusoidal variations. When a limited number of sinusoid cycles are measured, the superimposed variations can bias the phase shift. This is evident, for instance, in the 15 GHz OVRO light curve of PKS 2131–021 in Fig. 1. One can see by eye that if the dashed orange curve, representing the best-fit sine wave to the OVRO data during the period when ALMA data are available, were continued half a cycle to the left, such that it extended into ~2010–2014, it would not line up perfectly with the data points due to superimposed variations during this time range. Another feature to note in this plot is the fluctuation of the ALMA and ACT data points above the sine curve in the year 2018: one sees the *same* trend at all the mm frequencies (Fig. 2), which also appears to be present in the 15 GHz OVRO data earlier, at 2017.5 (Fig. 1). In other words, random, non-sinusoidal fluctuations can be coherent across frequency bands. All these variations contribute to the uncertainty of the absolute phase measurement, and will be larger the smaller the number of cycles.

K24 distinguish two important types of variations, which we summarise here. ‘Type-A variations’ are common across different observing frequencies, only shifted by the same amount as the sinusoid phase shift; an example was described at the end of the previous paragraph. ‘Type-B’ variations, on the other hand, are unique at each frequency,

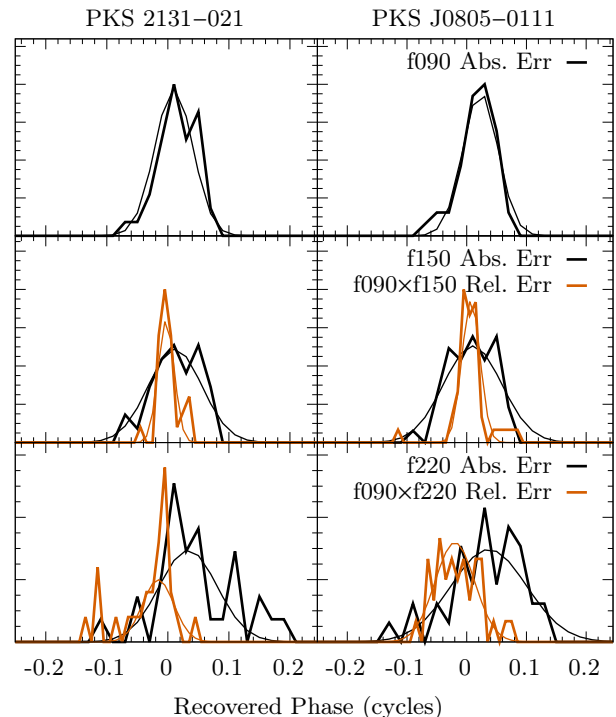


Fig. B.1. Normalised histograms of recovered phases (thick lines), t_0 , as well as phase differences, $t_{0,v_1} - t_{0,v_2}$. The overlaid Gaussian curves (thin lines) have widths derived from the median absolute deviation of the distribution, which serve as estimates of the absolute and relative phase errors. The errors are listed in Table B.2.

or show a different frequency dependence from that of the sinusoid. If the light curves are dominated by Type-A variations, which could arise from variable fuelling of the jet, then the *relative error* of the phase difference between frequencies will be considerably smaller than the absolute error, since all frequencies will have the same bias in the absolute phase determination; if, on the other hand, they are dominated by Type-B variations, which could be caused by local disturbances along the jet, then the uncertainty of the relative phase difference would be commensurate with the uncertainty of the absolute phase.

Whether Type-A or Type-B variations dominate is an empirical question, and K24 conclude that they cannot make a firm estimate given the lack of a large sample of multi-frequency light curves of SMBHB candidates. Thus, our fitting procedure in Sec. 3.1, while it includes a parameter for correlated noise within a single light curve, does not assign any noise covariance between different light curves; they are essentially independent fits, all using the same period that is measured in the OVRO data. As K24 point out, if all of the variations are Type-A, then any bias on the fits will be the same at all frequencies, and the independent fits will provide a good uncertainty estimate.

Appendix B.2: Method

For our ACT light curves, we can make progress on the empirical front using our preliminary catalog of 205 bright AGN multi-frequency light curves (see Sec. 2.1). Under the assumption that the Type-A and Type-B variations affect

Table A.1. Sine-wave fit results for PKS 2131–021.

Parameter	OVRO 15 GHz	ALMA 91.5 GHz	ALMA 103.5 GHz	ALMA 345 GHz
P (days)	2003 ± 19 (fixed)			
A (Jy)	0.4385 ± 0.0059	0.3170 ± 0.0066	0.2995 ± 0.0067	0.1386 ± 0.0060
ϕ_0 (rad)	3.725 ± 0.016	3.268 ± 0.027	3.242 ± 0.028	2.886 ± 0.054
S (Jy)	2.2022 ± 0.0045	1.4227 ± 0.0054	1.3536 ± 0.0054	0.7194 ± 0.0044
ξ (Jy)	0.0696 ± 0.0035	0.0731 ± 0.0043	0.0717 ± 0.0042	0.0466 ± 0.0044
$\Delta\phi_0$ (cycles)	0	-0.0727 ± 0.0050	-0.0769 ± 0.0052	-0.1336 ± 0.0090
$\Delta\phi_0$ (days)	0	-145.6 ± 9.9	-154 ± 10	-268 ± 18

Notes. The period, P , was determined from an initial fit including only the OVRO data in the range 57779 < MJD < 60053. The joint fit including OVRO and the three ALMA light curves kept the period fixed at this best fitting value. The fit uncertainties do not account for systematics due to superimposed, shorter term variations (see Appendix B.1). The reference time for the phase, in MJD, is $t_0 = 59000$. The phase shift, $\Delta\phi_0$, is defined in Eq. 2.

Table B.1. Properties of SMBHB candidate ACT light curves

AGN	Freq. (GHz)	span ^a (days)	SNR _{sin}	SNR _{var}
PKS 2131–021 <i>period: 1931 d</i>	95	2084	3.2	2.8
	147	2197	2.5	2.6
	225	1837	1.1	1.9
PKS J0805–0111 <i>period: 1402 d</i>	95	1695	2.8	2.0
	147	1708	2.1	1.6
	225	1447	1.0	1.0

Notes. SNR_{sin} is the amplitude of the sine relative to its residuals (Eq. B.2, and SNR_{var} is the rms of the residuals relative to the average flux uncertainty (Eq. B.3)

(^a) The light curve length, ignoring gaps.

blazars that are not SMBHB candidates in the same way that they affect the two SMBHB candidates discovered thus far – which we stress is untested – we can estimate the absolute and relative phase shift uncertainties by injecting a sinusoid into the light curves:

$$f'(t) = f(t) + \text{SNR}_{\text{sin}} \sigma_f \sin\left(\frac{2\pi t}{P_0}\right), \quad (\text{B.1})$$

where f is the original light curve, σ_f is the standard deviation of the original light curve, SNR_{sin} is the signal-to-noise ratio (SNR) of the sinusoid and P_0 its period. When we have multiple measurements at the same MJD at the same frequency (i.e., from different arrays), we use their mean value. Note that we have factored the amplitude of the sinusoid into a SNR term (SNR_{sin}) and a noise term (σ_f) in order to use sine waves of similar SNR as our SMBHB candidates. Table B.1 shows the SNR of the sinusoids in our SMBHB candidates at each frequency, which we obtained by subtracting the best-fitting sinusoid from the SMBHB candidate, measuring the standard deviation of its residuals, σ_{resid} , and calculating:

$$\text{SNR}_{\text{sin}} = \frac{A}{\sigma_{\text{resid}}}. \quad (\text{B.2})$$

where A is the best-fitting amplitude of the sine wave. In the same table, we also list the SNR of the residuals after subtracting the sine wave with respect to the flux uncertainties:

$$\text{SNR}_{\text{var}} = \frac{\sigma_{\text{resid}}}{\bar{\sigma}_f} \quad (\text{B.3})$$

where $\bar{\sigma}_f$ is the mean value of the flux uncertainties in the light curve. This variable captures the SNR of the non-sinusoidal residuals.

We estimate the uncertainty in phase measurements by fitting a sinusoid to $f'(t)$,

$$s(t) = A \sin\left[\frac{2\pi(t - t_0)}{P_0}\right] + b, \quad (\text{B.4})$$

where A , t_0 and b are free parameters. A non-zero best-fitting t_0 represents an error in recovering the input phase. We carry out this fit on our ensemble light curves (with the SMBHBs excluded from the sample), where the injected light curves have P_0 and SNR_{sin} set to the values in Table B.1. We make two cuts on the ensemble of light curves. First, we require that the time span covered by each light curve be at least 95% that of PKS 2131–021 or PKS J0805–0111 (see Table B.1) so that the length of the sine wave being fitted is representative of our SMBHB candidates. Second, we only include light curves which have SNR_{var} < 5, where here, SNR_{var} = $\sigma/\bar{\sigma}_f$, with σ being the standard deviation of the original light curve. We explain the rationale for this cut in Sec. B.4, below. After both cuts, about 16 to 24% of the original 204 light curves remain, depending on the frequency and the AGN being studied (see ‘Count’ in Table B.2).

With the final ensemble in hand, we use the `curve_fit()` routine in the optimization package of SCIPY to do a non-linear least squares fit to Eq. B.4 for each light curve and obtain a distribution of t_0 at each of the ACT frequencies. The width of this distribution indicates the absolute error on the phase shift. The width of the distribution of the difference of the recovered fits in the light curves at two frequencies, $\Delta t_{\nu_1, \nu_2} = t_{0, \nu_1} - t_{0, \nu_2}$, indicates the relative error on the phase shifts between frequencies ν_1 and ν_2 .

Appendix B.3: Results and discussion

The distributions of our phase fits are shown in Fig. B.1. We estimate the width of the distribution using the median absolute deviation (MAD) statistic, since it is robust to outliers, and report errors as $\sigma = \text{MAD}/0.6745$, where the numeric factor is the conversion to the Gaussian width for a normal distribution.¹⁵ These error estimates are listed in

¹⁵ The MAD is the distance between the 50th and 75th percentiles (assuming the distribution is symmetric), which for a Gaussian is equal to $\sqrt{2} \text{erf}^{-1}(\frac{1}{2})\sigma \approx 0.6745\sigma$.

Table B.2. Results of phase shift uncertainty analysis using sine-wave injections into ACT AGN light curves.

AGN	Freq. (GHz)	Count ^a	Empirical Abs. ^b (%)	Freq. Pair (GHz–GHz)	Empirical Rel. (%)	MCMC (%)
PKS 2131–021	95	41	3.1	95–147	1.3	0.60
	147	36	4.4	95–225	2.6	1.8
	225	32	4.7	147–225	3.3	1.8
PKS J0805–0111	95	47	2.9	95–147	1.5	0.52
	147	48	4.9	95–225	3.3	1.5
	225	39	6.3	147–225	4.0	1.5

Notes. The MCMC error is obtained via the method described in Sec. 3.1, and the empirical absolute and empirical relative errors are estimated by injecting known, artificial sine waves into real AGN light curves and measuring how well their phases can be recovered with respect to the input phase (absolute error) and with respect to the best fit in other frequencies (relative error). Note that it is not appropriate to compare the MCMC error directly against the absolute error; see text for details.

(^a) Number of AGN used (see text). (^b) All errors are quoted as percentage of a cycle, i.e., $100 \times \Delta P/P_0$.

Table B.2. There is broad agreement between the scenarios representing the two SMBHB candidates: the absolute uncertainty is about 3%, 4–5% and 5–6% of a cycle for 95, 147 and 225 GHz, respectively, and the relative uncertainty between 95 and 147 GHz is about 1.5% and is 3–4% between 95/147 and 225 GHz.

The uncertainties from the MCMC fits (Sec. 3.1) are also shown in Table B.2. Here, we have assumed the hypothesis that the SMBHB light curves are dominated by Type-A variations, such that the MCMC uncertainties represent purely *relative errors*, and have added in quadrature the uncertainties in ϕ_0 provided in Tables 1 and 2 for the three pairs of ACT frequencies. The MCMC uncertainties are ~ 2 – 3 times smaller than our empirical estimates. Given our current limited understanding of SMBHB light curve properties, we consider MCMC and empirical relative uncertainties to be in broad agreement. The MCMC uncertainties could be artificially low if Type-B variations are non-negligible. On the other hand, the empirical analysis is based on the assumption that injecting sine waves into non-SMBHB AGN light curves provides an accurate simulation of SMBHB light curves, or, in other words, that Type-A and Type-B variations behave the same way in SMBHB and non-SMBHB AGN. If this assumption is faulty then the resulting errors could be inflated; furthermore, the sample size is modest. For these reasons, the MCMC uncertainties may well be appropriate for SMBHBs, and that they appear to be reasonable given the fit of the simple quadratic curve in Fig. 4. In the end, the main results of this paper are not sensitive to the exact size of the error bars, but the work in this Appendix demonstrates the need for more data to better understand the uncertainties in SMBHB sine fits.

Appendix B.4: Further tests on phase uncertainty estimates

Varying SNR_{sin} : The left panel of Fig. B.2 shows the effect on the relative uncertainties of varying the value of SNR_{sin} injected into the ensemble of light curves. Of particular interest is that the 95–225 GHz and 147–225 GHz uncertainties based on the fiducial SNR_{sin} values, taken from our real SMBHB candidate (Table B.1), are essentially the same if *no* sine wave is inserted into light curves in our ensemble, i.e., $\text{SNR}_{\text{sin}} = 0$. This means that our errors relative to the 225 GHz light curves, which only have $\text{SNR}_{\text{sin}} \approx 1$, are dominated by Type-A variations: it is not so much the phase shift in the sine wave that is being measured as the

shift in the Type-A variations. On the other hand, the 95–147 GHz relative uncertainty, where the SMBHB candidate has $\text{SNR}_{\text{sin}} \approx 2.5$ – 3 , is significantly smaller than if SNR_{sin} is set to zero. When SNR_{sin} is raised to 3 for light curves at all frequencies, the relative errors between all frequencies is $\approx 1\%$, and is reduced as SNR_{sin} increases, as expected.

Varying SNR_{var} : The right panel of Fig. B.2 explores how well the relative uncertainty can be measured for different SNR_{var} . Our SMBHBs have comparatively small SNR_{var} : at 95 GHz, $\text{SNR}_{\text{var}} = 2.8$ and 2.0 for PKS 2131–021 and PKS J0805–0111, respectively, compared to the median of 7.9 for the 204 other AGN in the ensemble. Effectively, this means that the residuals of the SMBHB candidates exhibit lower variations than are found in the other, non-SMBHB light curves. As the figure shows, when all AGN are used to estimate the relative light curves, the errors relative to 225 GHz are higher than if we perform a cut on SNR_{var} , such that the AGN included in the sample have variations that are more representative of the SMBHB candidates. On the other hand, the 95–147 GHz relative error is not sensitive to any cuts on SNR_{var} . Again, the interpretation is that when $\text{SNR}_{\text{sin}} \geq 2$, the sine wave is larger than the other variations, and thus the relative phase errors are not very sensitive to the non-sinusoidal variations; this is not the case when $\text{SNR}_{\text{sin}} \sim 1$. With our limited sample, doing a cut for $\text{SNR}_{\text{var}} < 3$ at 95 GHz, which would best represent our SMBHB candidates, only leaves 17 AGN in the sample. We therefore opt for a cut on $\text{SNR}_{\text{var}} < 5$, which more than doubles the number of available AGN (see the ‘Count’ column in Table B.2) while not significantly altering the resulting error estimates, as can be seen in Fig. B.2. Finally, as a consistency check, for our fiducial cut of $\text{SNR}_{\text{var}} < 5$ we also did a test where we set $\text{SNR}_{\text{sin}} = 3$ for all frequencies, and found results similar to the left-hand panel of Fig. B.2, where no cut on SNR_{var} was used. This confirms the point made above, that when $\text{SNR}_{\text{sin}} \geq 2$, non-sinusoidal variations do not impact the uncertainty much.

Including phase shifts in injected sine waves: An inaccuracy in our empirical error estimates is that we inject sine waves with the same phase at all frequencies. In reality, we know from our two SMBHB candidates that they are slightly phase shifted. To test whether neglecting this effect affects our error estimates, we introduced different relative phase

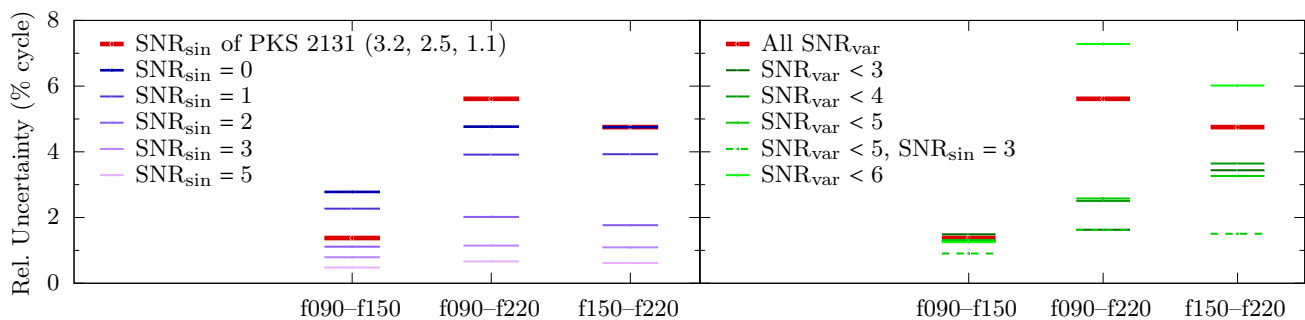


Fig. B.2. Relative errors calculated subject to various SNR values used in the sine waves injected into our ensemble of AGN light curves. *Left:* In this panel, we compare the relative errors obtained when SNR_{sin} is set to the value from PKS 2131–021 (heavy red lines), to when SNR_{sin} is set, at all frequencies, to 0, 1, 2, 3 or 5 (blue lines). *Right:* Relative errors obtained when AGN are cut from the sample based on their SNR_{var} at 95 GHz (green lines), compared to what is obtained when all AGN are used (red lines). The dashed green line shows results when both an $\text{SNR}_{\text{var}} < 5$ cut is applied and SNR_{sin} is set to 3 at all frequencies.

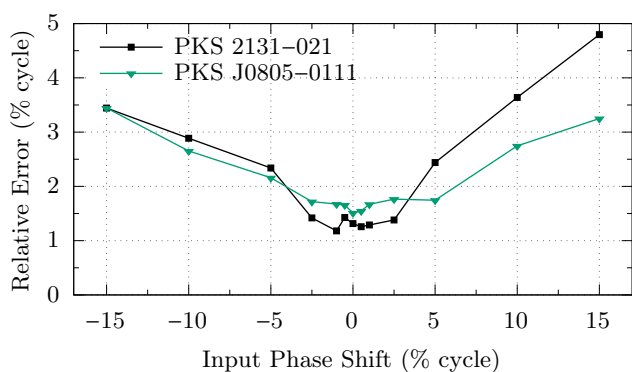


Fig. B.3. The effect of adding relative phase shifts into the injected sinusoids. Shown here is the 95–147 GHz relative error, where the sine wave injected into the 147 GHz light curve has been shifted relative to the 95 GHz light curve by the amount shown on the x-axis. Results for sine waves having properties of each of PKS 2131–021 and PKS J0805–0111 (see Table B.1) are shown.

shifts into the injected sine waves and repeated the analysis. As for our fiducial error estimates, we apply a cut of $\text{SNR}_{\text{var}} < 5$. Fig. B.3 shows the results for the 95–147 GHz relative uncertainty, and shows that for phase shifts $\lesssim 2.5\%$ of a cycle, the effect is negligible. Since the phase shifts in our SMBHB are smaller than this, we conclude that neglecting this in our fiducial results (Table B.2) is not important. The results for the 95–225 GHz and 147–225 GHz uncertainties are considerably noisier but broadly similar.¹⁶

Appendix C: Optical light curve periodicity

We analyzed the joint CRTS V-band and ZTF g-band light curve of PKS 2131–021 with the generalized Lomb-Scargle (GLS) periodogram (Lomb 1976; Scargle 1982; Zechmeister & Kürster 2009). The strongest peak in the periodogram is at a period of 1711 days and a power of 0.22 (normalized between 0 and 1, where 1 would imply a perfect sine fit). The period is within the 3σ range, 1657.5–1854.1 days, of the periodicity detected in the OVRO 15 GHz data as re-

ported in Table 1 of K24. The low GLS peak power is a result of the strong red-noise component in the data. We estimate¹⁷ a power-law index of $\beta_{\text{opt}} = 1.5$ of the red-noise power spectral density (PSD $\sim \nu^{-\beta}$, where ν is the temporal frequency). Compared to the 15 GHz radio light curve with a PSD index $\beta_{\text{radio}} = 1.8$ (O22), the optical PSD is flatter, implying stronger variability on short time scales.

GLS analysis of the joint CRTS and ZTF g-band data gives a period of 1711 days and a power of 0.22. ZTF alone gives a period of 1728 days and a power of 0.23 whereas CRTS alone does not identify a period consistent with the radio period. In fact, the strongest peaks in the CRTS periodogram come from the sampling window associated with the CRTS observing cadence. The effect of the CRTS cadence can be demonstrated by downsampling the ZTF data (median $\Delta t = 3$ days) to the CRTS cadence (median $\Delta t = 15$ days): a joint analysis gives a period of 1724 days and a power of 0.36 but the false alarm probability (FAP) from bootstrap analysis shows the result is no longer significant. Although the FAP is not relevant for assessing the statistical significance of any peak against a correlated noise background, it can be used to assess the effect of cadence on a signal. In this case, the shorter cadence of ZTF data improves the statistical detectability of a signal in the joint data to a significant level, with a p-value of 0.002, as compared to a p-value of 0.414 for joint data with the same median cadence.

We perform different four tests to evaluate the feasibility of using optical data to robustly detect sinusoidal variations in PKS 2131–021.

Test 1: We use the procedure described in Appendix A of O22 to estimate the significance of the detected periodicity. Our null hypothesis is that the detected periodicity is a spurious result of a pure red-noise stochastic process. We simulate 20 000 artificial light curves that have the same PSD, PDF, time sampling and observational noise characteristics as the optical light curve. We use the `1csim` python package (Kiehlmann 2023) based on the algorithm of Emmanoulopoulos et al. (2013). For the original data and each simulation we calculate the GLS periodogram, identify the strongest peak, and use the remaining simulations to esti-

¹⁶ The 95–225 GHz result for PKS 2131–021 is the noisiest, with the uncertainty estimate varying by a factor of 2 for shifts between -2% and 2% .

¹⁷ We used this Python package for the power spectral density analysis: https://github.com/skiehl/psd_analysis.

Table B.3. Generalized Lomb-Scargle test results of the optical light curves of PKS 2131–021.

Test	Description	Data	GLS period (days)	GLS power	p-value
1	Independent of radio data	CTRS+ZTF	1711	0.22	0.937
2	Prior knowledge of radio period	CTRS+ZTF			0.047
3	Prior knowledge of radio period	ZTF			0.065
4	Prior knowledge of radio period	CRTS			0.079

Notes. The GLS peak in the OVRO 15 GHz light curve has power $\mathcal{P}_{\text{peak}} = 0.83$, and p-value = 5.3×10^{-5} (K24).

mate the probability that the red-noise process produces a power at least as strong as detected at the peak frequency. This probability is used as test statistic in the next analysis step. Among all simulations we count those that have a test statistic at least as low as that derived from the original light curve, which gives us the *global p-value*. This global p-value takes into account that spurious periodic signals may occur at any frequency in the frequency range tested by the GLS periodogram. We refer to Appendices A in O22 and D24 for a detailed description of the procedure. We find a global p-value of 0.937. Therefore, we cannot reject the null hypothesis of a red-noise process producing a spurious periodicity.

Test 2: When we take our prior knowledge of the strongly significant radio periodicity (p-value = 5.3×10^{-7} ; K24) into account, we can ask the following question: How likely is it that the red-noise process produces a GLS peak at least as strong as observed in the optical data with a period in the 3σ range of the radio period (1657.5–1854.1 days, K24)? Among the 20 000 simulations we count 934 that fulfill these criteria, corresponding to a p-value of 0.047. Even with the optical period falling close to the radio period, we cannot confidently rule out the red-noise hypothesis.

Stronger support for the true existence of a period in the optical data consistent with the period seen in the radio data comes from the fact of how well the phase of the optical periodicity ties into the phase-frequency relation discussed in K24.

Tests 3 and 4: We also analysed the CRTS and ZTF data independently. The GLS periodogram of the ZTF data shows the strongest peak at a period of 1728 days. The periodogram of the CRTS also shows a peak near the radio periodicity. However, there are several other spurious peaks that do not correspond to significant detections. Using the same approach as for Test 2 above on the individual light curves, in Table B.3 we see that the combined CRTS+ZTF light curve provides the most evidence against the null hypothesis. This is expected as the joint data cover more cycles of the long time-scale periodicity, hidden in the red-noise component, that produces strong variability on shorter time-scales.

The foregoing analyses demonstrates that it can be more complicated to detect a periodicity in optical blazar light curves from current surveys, since the short-term variability is stronger than at radio-submm frequencies. Thus more extended long-term observations with higher cadence are needed to reveal periodicities in the presence of the red-noise component